IEEE Photonics Journal
An IEEE Photonics Society Publication

Open Access

Characterization of Insertion Loss and Back Reflection in Passive Hybrid Silicon Tapers

Volume 5, Number 2, April 2013

Géza Kurczveil
Paolo Pintus
Martijn J. R. Heck
Jonathan D. Peters
John E. Bowers

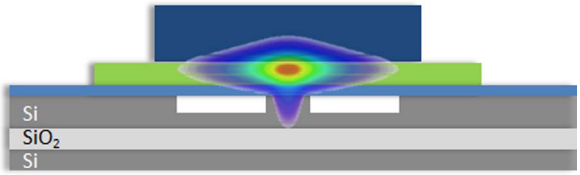

DOI: 10.1109/JPHOT.2013.2246559
1943-0655/$31.00 ©2013 IEEE

IEEE photonics SOCIETY

IEEE

Characterization of Insertion Loss and Back Reflection in Passive Hybrid Silicon Tapers

Géza Kurczveil,[1,2] Paolo Pintus,[1,3] Martijn J. R. Heck,[1] Jonathan D. Peters,[1] and John E. Bowers[1]

[1]Department of Electrical and Computer Engineering, University of California, Santa Barbara, CA 93106 USA
[2]HP Labs, Palo Alto, CA 94304 USA
[3]Scuola Superiore Sant'Anna, 56124 Pisa, Italy

DOI: 10.1109/JPHOT.2013.2246559
1943-0655/$31.00 ©2013 IEEE

Manuscript received January 13, 2013; revised February 1, 2013; accepted February 6, 2013. Date of publication February 11, 2013; date of current version February 26, 2013. Corresponding author: G. Kurczveil (e-mail: geza_k@ece.ucsb.edu).

Abstract: The optical properties of two hybrid silicon taper designs are investigated. These tapers convert the optical mode from a silicon waveguide to a hybrid silicon III/V waveguide. A passive chip was fabricated with an epitaxial layer similar to those used in hybrid silicon lasers. To separate optical scattering and mode mismatch from quantum-well absorption, the active layer in this paper was designed to be at 1410 nm, to allow measurements at 1550 nm. Using cutback structures, the taper loss and the taper reflection are quantified. Taper losses between 0.2 and 0.6 dB per taper and reflections below −41 dB are measured.

Index Terms: Optoelectronics, optical amplifiers, semiconductor lasers, photonic integrated circuits.

1. Introduction

The integration of III/V materials on silicon is an area of active research interest as it combines low loss silicon passive devices with direct band-gap active devices for, e.g., light generation, gain, modulation, and photodetection [1], [2]. There are a number of approaches for integrating direct band-gap materials on silicon. The first is to bond fabricated active devices to the silicon wafer [3]. Since this approach requires careful alignment of each component, it does not scale well to larger more complex photonic integrated circuits that might require upward of ten bonds. The growth of III/V material [4], [5] is a more scalable approach. However, growth of III/V on silicon is still in its infancy, and this technology is not suitable yet for making high-yield and high-performance devices.

The bonding of III/V materials on silicon is a likewise scalable approach [6]. Using such wafer bonding approaches, complex large-scale integrated PICs have been demonstrated in the hybrid silicon platform [7], [8]. Alignment tolerances for wafer or die bonding are generally relaxed to hundreds of micrometers because active devices are lithographically defined after bonding. This makes wafer bonding an attractive choice for integrating actives with silicon.

Since the optical mode profiles in silicon and hybrid silicon waveguides are different, an essential part of the hybrid silicon integration platform is a mode converter. Examples of these mode profiles are shown in Fig. 1. A mode converter transfers the optical mode from the passive silicon waveguide to hybrid silicon waveguides, where the mode overlaps with or is contained within the III/V layer. For efficient performance, the mode converter should have negligible loss when compared to the loss budget of the optical link, i.e., below 0.5 dB for most target applications. In addition, for

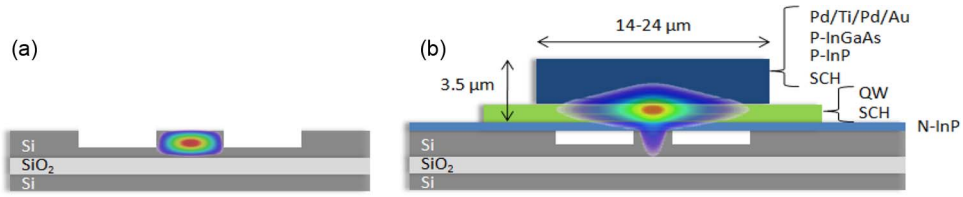

Fig. 1. (a) Optical mode in passive silicon waveguide. (b) Optical mode in hybrid silicon waveguide.

applications that are sensitive to feedback, such as PICs containing lasers, reflections from the mode converter have to be below −50 dB [9].

In previous work, abrupt junctions and tapered mode converters have been studied. In [10], junctions with an abrupt 7° angled III/V interface from the silicon waveguide to the hybrid waveguide were simulated. Losses were calculated to be 1.2 dB per transition, with reflections of −30 dB. Tapered mode converters were realized in, e.g., [1], [11], and [12]. Simulations show that losses can be below 0.5 dB per transition for taper tip widths of 400 nm and reflections can be below −50 dB [14]. These results show that tapers are in principle the most promising option for integrating hybrid silicon devices on a passive silicon platform.

A thorough analysis of such tapers would require characterization of all the loss mechanisms that contribute to the taper performance. These are free-carrier absorption due to doping and carrier injection, sidewall and surface scatter losses, modal mismatch, and intraband absorption (or gain) due to unpumped (pumped) quantum wells (QWs). In this paper, for the first time, we present a thorough investigation of the passive loss contributions by using QWs with a blue-shifted band gap, thereby eliminating intraband absorption effects. Such an approach provides essential insight to achieve complete understanding and, hence an optimized taper design since, in active hybrid silicon devices, intraband absorption effects cannot be isolated from passive loss contributions. While characterizing taper losses using 1550-nm QWs is possible by using a longer wavelengths (> 1600 nm, where the device is transparent), the equipment needed for the characterization is more readily available in the 1550-nm regime. As a result, blue-shifted QWs were used.

In this paper, we will first describe the taper designs and fabrication used in this paper in Section 2. Taper losses and reflections will be presented and discussed in Sections 3 and 4, respectively. In Section 5, we will conclude with an overview and a design recommendation.

2. Device Design and Fabrication

In this paper, tapers will be studied, which can convert the optical mode in a silicon waveguide to a hybrid mode and vice versa, as shown in Fig. 1. The taper designs have to be compatible with the processes normally used to fabricate hybrid silicon PICs, e.g., as outlined in [12]. In this process, silicon waveguides were first defined on SOI wafers by etching 400-nm deep trenches into a 700-nm thick silicon layer. A 1-μm-thick buried-oxide layer was used. Vertical outgassing channels were then patterned to promote the adhesion of the III/V layer to the silicon. Next, the III/V layer was transferred to the SOI wafer by means of wafer bonding. In three etch steps, tapers were defined in the III/V layers. For the first taper level, a metal hard mask was used to keep the process identical to the one outlined in [12]. The III/V epitaxial layer stack used in this paper is summarized in Table 1. The QWs in this paper were grown at a band gap corresponding to a wavelength of 1410 nm. This made the devices transparent at 1550 nm, where the transmission measurements were conducted. The refractive index of these blue-shifted QWs was similar to the 1550-nm QWs used in previous studies. This was verified by measuring the group index of the blue-shifted hybrid waveguides and comparing it to previously fabricated hybrid waveguides using 1550-nm QWs. Furthermore, the mode shape in the hybrid region as imaged by an infrared camera revealed a hybrid mode that looked similar to the one in 1550-nm devices.

Two different taper types were designed and studied. These are schematically shown in Fig. 2. In the first taper type, i.e., Type 1, the three taper levels start within 2.4 μm of each other, and the final taper is 80 μm long. The mesa in this design is 24 μm wide. Devices using such tapers were

TABLE 1

III/V epitaxial layers used in this paper. The QW PL peak is at 1410 nm

Layer	*Material*	*Thickness [nm]*	*Doping*	*Taper level*
P metal	Pd/Ti/Pd/Au	1370	-	1
P contact	$In_{0.53}Ga_{0.47}As$	100	$> 1{\cdot}10^{19}$ P	1
Cladding	InP	1500	$1{\cdot}10^{18}$ P	1
SCH	$Al_{0.13}Ga_{0.34}In_{0.53}As$	125	$1{\cdot}10^{17}$ P	1
QW (8x)	$Al_{0.09}Ga_{0.46}In_{0.45}As$	7	n.i.d	2
Barrier (9x)	$Al_{0.06}Ga_{0.29}In_{0.65}As$	10	n.i.d	2
SCH	$Al_{0.13}Ga_{0.34}In_{0.53}As$	125	$1{\cdot}10^{17}$ N	2
N contact	InP	110	$1{\cdot}10^{18}$ N	3
Superlattice	$In_{0.85}Ga_{0.15}As_{0.33}P_{0.67}$	7.5	$1{\cdot}10^{18}$ N	3
	InP	7.5	$1{\cdot}10^{18}$ N	3
	$In_{0.85}Ga_{0.15}As_{0.33}P_{0.67}$	7.5	$1{\cdot}10^{18}$ N	3
	InP	7.5	$1{\cdot}10^{18}$ N	3
Bonding layer	InP	10	$1{\cdot}10^{18}$ N	3

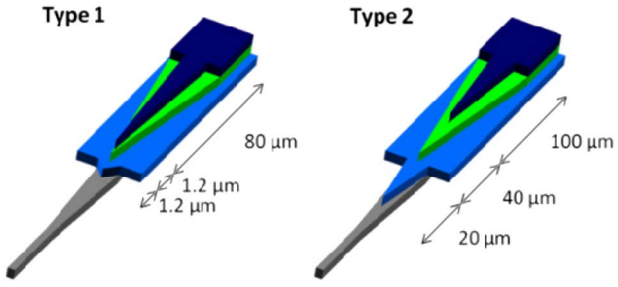

Fig. 2. Two taper types investigated in this paper. Three taper levels are shown: P-InP, top SCH (dark blue), QWs and bottom SCH layer (green), and N-InP, Super Lattice and bonding layers (light blue). The silicon waveguide is shown in gray.

reported previously in [10]. In the second taper type, i.e., Type 2, the three taper levels start within 60 μm of each other, and the final taper is 100 μm long. The larger offsets in the taper levels are expected to convert the mode more gradually, resulting in lower losses and reflections. Furthermore, the mesa in this design is 14 μm wide to support fewer higher order modes than the Type-1 design. Devices using such taper designs were reported in [12].

The fabricated devices had 7° angled input and output silicon waveguides to reduce facet reflections, with a width of 2 μm to reduce coupling loss to 9.5 dB per waveguide facet. The waveguide was then tapered to 0.8 μm for single mode light propagation. For 100 μm before the start of the first III/V taper tip, the SOI waveguide is tapered to 2 μm to reduce the alignment tolerance of the taper with respect to the silicon waveguide and possible taper reflections (see Fig. 3). In both taper types, the silicon waveguide is tapered to either 1.0 μm or 1.5 μm at the start of the final III/V taper level. These two different silicon waveguide widths give different QW confinement factors (15.6% and 14.4%) in the hybrid waveguide, as shown in Fig. 4. This effect can be used to change the gain of a hybrid silicon semiconductor optical amplifier (SOA) and to optimize it for, e.g., high gain or high saturation power [1]. No metallization was done as the devices did not require electrical pumping due to the band-gap-shifted QWs. Omitting these steps increased device yield and decreased device footprint, leading to better and increased statistics.

To quantify taper losses, two cutback-on-chip structures were designed, as shown in Fig. 3. The device array in Fig. 3(a) consists of several hybrid waveguides with lengths from 200 μm to 1800 μm. By plotting their insertion losses as a function of the hybrid length, the hybrid waveguide loss and

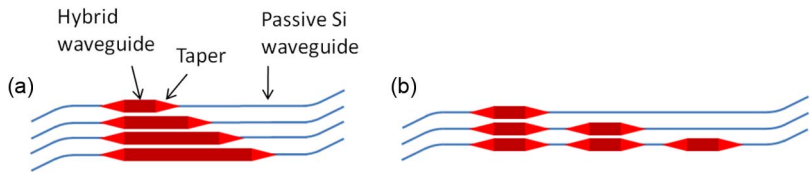

Fig. 3. (a) Cutback structures to determine hybrid waveguide loss. (b) Cutback structures to determine taper loss.

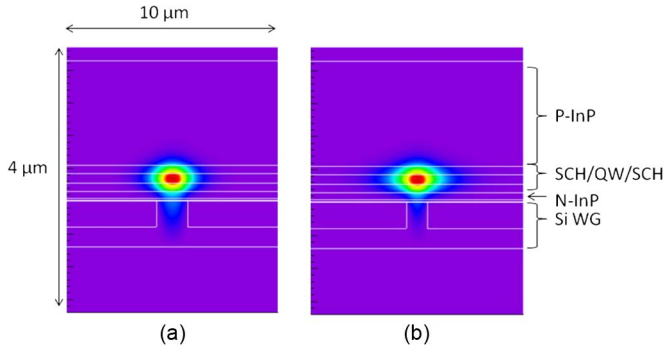

Fig. 4. Profile of a hybrid silicon mode using (a) a 1.5-μm-wide silicon waveguide and (b) a 1.0-μm-wide silicon waveguide. (Note the compressed horizontal axis.)

total insertion loss can be extracted, as explained below. In a similar way the insertion loss of devices with a 200-μm-long hybrid section can be extracted, using a design as shown in Fig. 3(b).

3. Taper and Hybrid Waveguide Loss

3.1. Experimental Setup

The insertion loss for the cutback-on-chip structures in Fig. 3 was measured by coupling transverse electric (TE) polarized light at 1550-nm wavelength with a lensed fiber into the device. Losses were typically around 9.5 dB per fiber–chip transition. The transmitted power was collected with another lensed fiber and was measured using an optical power meter.

3.2. Experimental Results

The cutback-on-chip data for the hybrid waveguides with varying lengths are shown in Fig. 5(a). The hybrid waveguide loss can be extracted by a linear fit through these data. The slope of the linear fit gives the hybrid waveguide loss or, to be precise, the additional loss of a hybrid waveguide as compared to a silicon waveguide of similar length. The intercept at $L = 0$ of this fit lumps in all additional losses of the setup, fiber–chip interfaces, passive silicon losses, and taper losses. The results on the hybrid waveguide losses are summarized in column 1 of Table 2. The hybrid waveguide loss is 1.7–2.0 dB/mm higher in hybrid waveguides with 1.0-μm silicon waveguides as compared to 1.5-μm silicon waveguides. This is due to the 1.0-μm waveguide devices having larger confinement factors in the highly doped III/V layers, especially the p-doped layer, thus increasing the optical loss. We hypothesize that the 0.5-dB/mm larger propagation loss in the 1.0-μm Type-1 device is due to the poorer confinement of higher order modes when compared to the narrower mesa in the 1.0-μm Type-2 devices. The hybrid waveguide losses measured in these devices are within the range of losses normally measured in monolithic III/V lasers that have similar QW confinements, with the 1.5-μm devices being on the lower end [13]. This illustrates the possibility for the hybrid silicon platform to make either high-gain SOAs or high-saturation power SOAs with low losses by changing the silicon width, i.e., by lithographic design only.

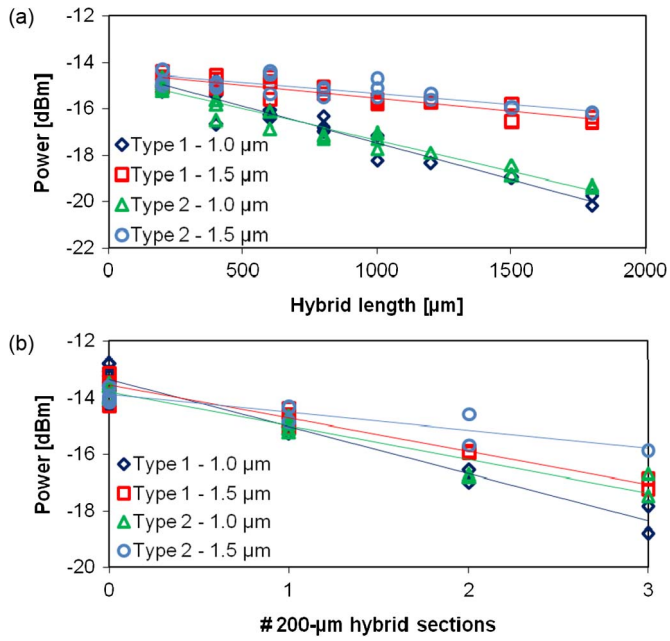

Fig. 5. (a) Cutback-on-chip data for hybrid waveguide loss. (b) Cutback data for taper loss.

TABLE 2

Summary of hybrid waveguide and taper losses. Note that type 1 devices use a 24-μm-wide III/V mesa while type 2 devices use a 14-μm-wide mesa resulting in different hybrid losses

	Hybrid loss [dB/mm]	*Taper loss [dB]*[1]	*Taper loss [dB]*[2]
Type 1 – 1.0 µm	3.2 ± 0.2	0.52 ± 0.05	0.47 ± 0.11
Type 1 – 1.5 µm	1.2 ± 0.1	0.47 ± 0.04	0.42 ± 0.07
Type 2 – 1.0 µm	2.7 ± 0.1	0.33 ± 0.05	0.43 ± 0.07
Type 2 – 1.5 µm	1.0 ± 0.1	0.22 ± 0.05	0.25 ± 0.08

[1] As determined from the slope in Fig. 6 (b).

[2] As determined from the offset in Fig. 6 (a).

The insertion loss as a function of the number of 200-μm-long hybrid sections is shown in Fig. 5(b). Straight lines were fit through the data to obtain the loss per section. By subtracting the corresponding hybrid waveguide losses, the taper (pair) loss was calculated. The resulting values are summarized in Table 2, column 2. Type-1 tapers have about 0.2-dB higher losses than Type-2 tapers. This is because Type-1 tapers convert the silicon mode more abruptly to the hybrid mode. For both taper types, 1.5-μm devices have lower taper losses. This is due to the optical mode having a larger overlap with the silicon waveguide as compared to the 1.0-μm devices. As a result, the mode does not have to be shifted up as much. Furthermore, in the 1.0-μm devices, the optical mode has a larger overlap with the higher loss III/V layers, increasing their taper losses.

An alternative way of measuring the taper loss is to subtract the insertion loss of a passive silicon waveguide from the intercept with $L = 0$ in Fig. 5(a). As stated above the intercept contains all loss contributions of setup, coupling and waveguide. When the insertion loss of a silicon waveguide is subtracted from a hybrid silicon waveguide (with $L = 0$), all loss contributions are eliminated from the equation, except for the taper loss. Table 2, column 3, shows the taper loss results obtained with this method. Agreement with the loss data of the previous method is observed, as can be seen by comparing columns 2 and 3.

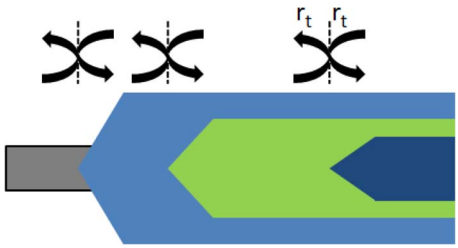

Fig. 6. Back-reflection coefficients at the silicon waveguide/hybrid waveguide interface.

3.3. Conclusion

The losses in both taper types were measured to be between 0.2–0.5 dB per taper where Type-2 tapers showed lower losses. These losses are significantly lower than the 1-dB–2-dB coupling loss values that are generally obtained in hybrid integration approaches [18], showing the clear advantage of this integration approach. However, for the integration of active hybrid silicon devices, where the QW band gap corresponds to the operating wavelength, the choice between Type 1 and Type 2 is less clear. If the QWs are etched in the second taper layer as was done in this paper, Type-2 devices will have a longer unpumped QW layer than Type-1 devices. This will lead to higher absorption in Type-2 devices. This is the subject of a future study.

Furthermore, the hybrid waveguide loss data illustrate the possibility for the hybrid silicon platform to make either high-gain SOAs or high-saturation power SOAs with low losses by lithographic design only. This is a unique feature of the hybrid silicon platform and will be essential when large-scale integration enables full systems on a chip, where these different functionalities will be required in a single PIC.

4. Taper Reflections

In SOAs, small back-reflections can cause lasing and/or a gain ripple, which, in extended cavity lasers, can introduce mode selection [14], [18], [19]. Especially when on-chip lasers are integrated with other devices in series further downstream the circuit, reflections need to be ideally below -50 dB to avoid laser linewidth broadening [9]. For a three-level taper, as studied here, having a finite tip radius, there are in principle three scattering interfaces per taper. This is shown schematically in Fig. 6. These coefficients have been simulated using the finite-difference method implemented by the commercial software FIMMWAVE [15] for the taper structures used in this paper. It was found that the largest reflections come from the first taper level (r_t in Fig. 6) and that their reflectivities are lower than -55 dB. Reflections from fundamental mode to (counter propagating) fundamental mode are considered here.

4.1. Experimental Setup

To quantify the reflections from the tapers, a method similar to the one presented in [16] was used where the transmission of the device as a function of wavelength was measured using a high-resolution optical spectrum analyzer (HR-OSA) with a resolution of 0.67 pm. For a device with straight silicon waveguide facets, the transmission spectrum will show the expected Fabry–Pérot ripples due to facet–facet reflections and a possible super-modulation of that spectrum due to cavities formed by additional taper reflections. These spectra can then be analyzed by plotting their Fourier transform (FT), where the different cavities will show up as distinct peaks. The data can then be fit to an analytical model that is based on transmission matrices.

To simplify the experimental approach, the devices from Fig. 3(a) are polished back on one side until the taper is completely removed and a hybrid facet is formed. On the other side, the silicon waveguide is polished to a straight (nonangled) facet. The devices now consist of a passive silicon waveguide, a tapered mode converter, and a hybrid waveguide, as shown in Fig. 7. The advantage

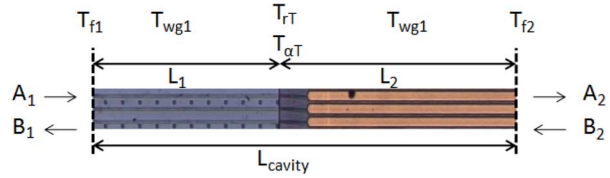

Fig. 7. Device used to determine taper reflections. Possible taper-facet cavities and transmission matrices of the individual components are indicated.

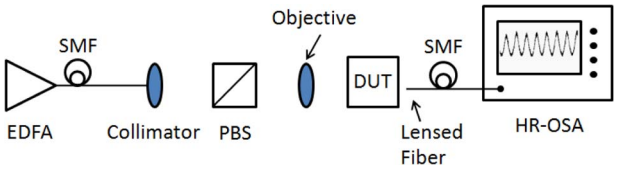

Fig. 8. Experimental setup used to measure taper reflections.

is that the taper tip only forms two extra cavities, L_1 and L_2, in addition to the cavity L_{cavity} that is defined by the two facets.

The wavelength-dependent transmission of the four different taper designs was measured using the setup, as shown in Fig. 8. The amplified spontaneous emission from an erbium-doped fiber amplifier (EDFA) was used as a broadband light source, which was connected to a collimator via single mode fiber (SMF). The TE polarization was selected with a polarizing beam splitter (PBS). A 50× microscope objective with a numerical aperture of 0.75 focused the beam of light onto the device. The transmitted light was collected by a lensed fiber that was connected to the HR-OSA. For three of the four taper designs, three devices were measured. For the fourth design (Type 1.0 μm), only one device was available. The system response was divided out by repeating the measurement without a device under test (DUT) to calibrate out the wavelength-dependent power from the EDFA. This did not introduce any additional peaks in FT in the region of interest (between 0 and L_{cavity}).

4.2. Optical Transmission Model

The device in Fig. 7 can be represented by a transmission matrix T, which is defined by

$$\begin{pmatrix} A_1 \\ B_1 \end{pmatrix} = \begin{pmatrix} T_{11} & T_{12} \\ T_{21} & T_{22} \end{pmatrix} \begin{pmatrix} A_2 \\ B_2 \end{pmatrix}. \tag{1}$$

See Fig. 7 for a definition for $A_{1,2}$ and $B_{1,2}$.

The transmission matrix T of the device can be broken up into the product of multiple elements for facet reflection $T_{f1,2}$, waveguide propagation $T_{wg1,2}$, and taper loss $T_{\alpha T}$ and reflection T_{rT}

$$T = T_{f1}\, T_{wg1}\, T_{rT}\, T_{\alpha T}\, T_{wg2}\, T_{f2} \tag{2}$$

where

$$T_{f1} = \frac{1}{\sqrt{1 - r_f^2}} \begin{pmatrix} 1 & -r_f \\ -r_f & 1 \end{pmatrix} \tag{3}$$

$$T_{wg1} = \begin{pmatrix} e^{\left(\alpha_1 + j\frac{2\pi n_{g1} L_1}{\lambda}\right)} & 0 \\ 0 & e^{-\left(\alpha_1 + j\frac{2\pi n_{g1} L_1}{\lambda}\right)} \end{pmatrix} \tag{4}$$

TABLE 3

Summary of variables used in the fitting of the OSA data

Variable	*Definition*	*Value*	*Source*
r_f	Facet field reflectivity	0.59	Simulation
α_1	Passive waveguide loss	5 dB/cm	Fit
α_2	Hybrid waveguide loss	Table 2	Fig. 6 (a)
r_t	Taper field reflectivity	-	Fit
α_t	Taper loss	Table 2	Fig. 6 (b)
n_{g1} (n_{g2})	Group index of passive (hybrid) waveguide	3.74 (3.76)	Fit
L_1 (L_2)	Passive (hybrid) waveguide length	Fig. 11	Measured

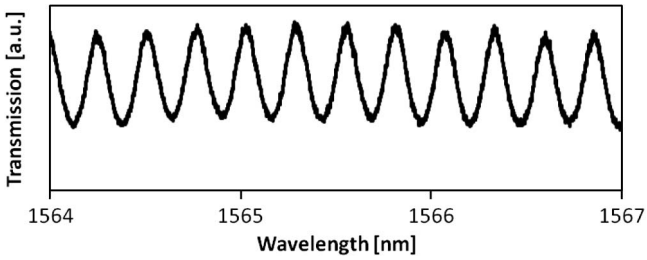

Fig. 9. Transmission spectrum of the Type-1 1.0-μm device.

$$T_{rT} = \frac{1}{\sqrt{1 - r_t^2}} \begin{pmatrix} 1 & -r_t \\ -r_t & 1 \end{pmatrix} \tag{5}$$

$$T_{\alpha T} = \begin{pmatrix} e^{\alpha_T} & 0 \\ 0 & e^{-\alpha_T} \end{pmatrix} \tag{6}$$

$$T_{wg2} = \begin{pmatrix} e^{\left(\alpha_2 + j\frac{2\pi n_{g2} L_2}{\lambda}\right)} & 0 \\ 0 & e^{-\left(\alpha_2 + j\frac{2\pi n_{g2} L_2}{\lambda}\right)} \end{pmatrix} \tag{7}$$

and the variables are defined in Table 3. Using this definition, the optical power transmitted by the device, the spectrum measured by the OSA, assuming the resolution of the OSA is far better than the fringe width, is given by

$$I_{\mathrm{OSA}} = \left(\frac{1}{T_{11} T_{11}^*}\right). \tag{8}$$

The fitting was done in the Fourier domain.

4.3. Experimental Results

For each device design, a 12-nm-long wavelength sweep was recorded. A 3-nm-long span of the transmission spectrum for the Type-1 1.0 μm device is shown in Fig. 9. The FT for the data and the corresponding fits are shown in Fig. 10. The FT of the transmission spectra do not always show distinct peaks at the locations of the taper-facet cavities. For those measurements, the taper reflection is in the noise level of the measurement. The resulting taper reflectivities are summarized in Table 4. Because some of the reflections are in the noise floor of the measurement, only an upper limit on the taper reflection can be given, and one cannot conclude which taper type exhibits smaller reflections.

The noise floor is due to the low received optical power at the HR-OSA. This was evidenced by a distortion of the valleys in Fig. 9 when the launched power was reduced by $\sim$3 dB. In addition,

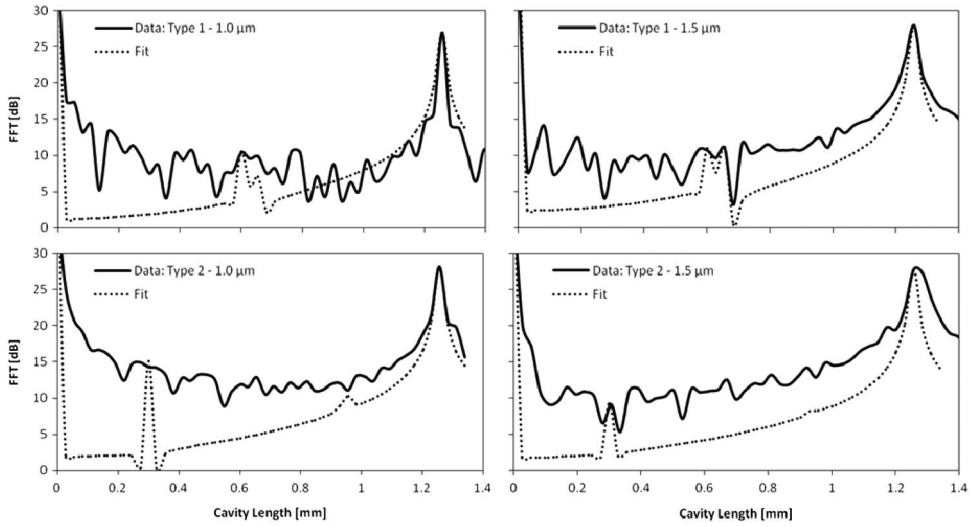

Fig. 10. FT of the transmission spectrum of four device and the corresponding fits.

TABLE 4

Summary of taper reflections. All results were limited by the sensitivity of the measurement setup and hence the shown values give an upper limit for the reflections. Only one data point was available for the Type-1 1.0-μm device, so no error bar could be calculated

	R_t [dB]
Type 1 – 1.0 µm	-44.0
Type 1 – 1.5 µm	-41.2 ± 1.7
Type 2 – 1.0 µm	-42.8 ± 1.9
Type 2 – 1.5 µm	-42.1 ± 2.0

scattered (unguided) light and sidewall roughness in the silicon waveguide [21] contributed to raising the noise floor in these measurements.

5. Conclusion

The taper losses and taper reflections for two types of hybrid silicon tapers have been investigated. Using cutback structures, taper loss between 0.22 and 0.57 dB has been measured. The Type-2 taper, which transforms the passive mode to the hybrid mode more gradually through longer tapers, exhibited smaller taper losses. Some of the taper reflections were in the noise floor of the measurement. However, for all four taper designs, taper reflections are at most −41 dB, which is good enough for applications that are not highly sensitive to feedback. These tapers can be used to efficiently integrate hybrid silicon amplifiers, modulators, and photodetectors with passive silicon circuitry.

References

[1] H. Park, Y.-H. Kuo, A. W. Fang, R. Jones, O. Cohen, M. J. Paniccia, and J. E. Bowers, "A hybrid AlGaInAs-silicon evanescent preamplifier and photodetector," *Opt. Exp.*, vol. 15, no. 21, pp. 13 539–13 546, Oct. 2007.
[2] Y. Tang, H. Chen, S. Jain, J. D. Peters, U. Westergren, and J. E. Bowers, "50 Gb/s hybrid silicon traveling-wave electroabsorption modulator," *Opt. Exp.*, vol. 19, no. 7, pp. 5811–5816, Mar. 2011.
[3] C. Gunn, "10 Gb/s CMOS photonics technology," in *Proc. SPIE*, 2006, vol. 6125, pp. 612501-1–612501-5.
[4] T. Mårtensson, C. P. T. Svensson, B. A. Wacaser, M. W. Larsson, W. Seifert, K. Deppert, A. Gustafsson, L. Reine Wallenberg, and L. Samuelson, "Epitaxial III–V nanowires on silicon," *Nano Lett.*, vol. 4, no. 10, pp. 1987–1990, Oct. 2004.

[5] T. Wang, H. Liu, A. Lee, F. Pozzi, and A. Seeds, "1.3-μm InAs/GaAs quantum-dot lasers monolithically grown on Si substrates," *Opt. Exp.*, vol. 19, no. 12, pp. 11 381–11 386, Jun. 2011.
[6] D. Liang, G. Roelkens, R. Baets, and J. E. Bowers, "Hybrid integrated platforms for silicon photonics," *Materials*, vol. 3, no. 3, pp. 1782–1802, Mar. 2010.
[7] J. K. Doylend, M. J. R. Heck, J. T. Bovington, J. D. Peters, M. L. Davenport, L. A. Coldren, and J. E. Bowers, "Hybrid III/V silicon photonic source with integrated 1D free-space beam steering," *Opt. Lett.*, vol. 37, no. 20, pp. 4257–4259, Oct. 2012.
[8] A. Alduino, L. Liao, R. Jones, M. Morse, B. Kim, W.-Z. Lo, J. Basak, B. Koch, H.-F. Liu, H. Rong, M. Sysak, C. Krause, R. Saba, D. Lazar, L. Horwitz, R. Bar, S. Litski, A. Liu, K. Sullivan, O. Dosunmu, N. Na, T. Yin, F. Haubensack, I. Hsieh, J. Heck, R. Beatty, H. Park, J. Bovington, S. Lee, H. Nguyen, H. Au, K. Nguyen, P. Merani, M. Hakami, and M. Paniccia, "Demonstration of a high speed 4-channel integrated silicon photonics WDM link with hybrid silicon lasers," presented at the OSA Integrated Photonics Research, Silicon Nanophotonics, Monterey, CA, USA, Jul. 25, 2010, Paper PDIWI5.
[9] R. W. Tkach and A. R. Chraplyvy, "Regimes of feedback effects in 1.5 μm distributed feedback lasers," *J. Lightw. Technol.*, vol. 4, no. 11, pp. 1655–1661, Nov. 1986.
[10] H. Park, A. W. Fang, R. Jones, O. Cohen, O. Raday, M. N. Sysak, M. J. Paniccia, and J. E. Bowers, "A hybrid AlGaInAs-silicon evanescent waveguide photodetector," *Opt. Exp.*, vol. 15, no. 21, pp. 13 539–13 546, Oct. 2007.
[11] M. Lamponi, S. Keyvaninia, C. Jany, F. Poingt, F. Lelarge, G. de Valicourt, G. Roelkens, D. Van Thourhout, S. Messaoudene, J.-M. Fedeli, and G. H. Duan, "Low-threshold heterogeneously integrated InP/SOI lasers with a double adiabatic taper coupler," *IEEE Photon. Technol. Lett.*, vol. 24, no. 1, pp. 76–78, Jan. 2012.
[12] G. Kurczveil, M. J. R. Heck, J. D. Peters, J. M. Garcia, D. Spencer, and J. E. Bowers, "An integrated hybrid silicon multiwavelength AWG laser," *IEEE J. Sel. Topics Quantum Electron.*, vol. 17, no. 6, pp. 1521–1527, Nov./Dec. 2011.
[13] J. Piprek, J. K. White, and A. J. SpringThorpe, "What limits the maximum output power of long-wavelength AlGaInAs/InP laser diodes?" *IEEE J. Quantum Electron.*, vol. 38, no. 9, pp. 1253–1259, Sep. 2002.
[14] H. Park, "Silicon Evanescent devices for optical networks and buffers," Ph.D. dissertation, Dept. ECE, Univ. California, Santa Barbara, CA, USA, Mar. 1, 2008.
[15] FIMMWAVE. [Online]. Available: http://www.photond.com/products/fimmwave.htm
[16] R. Hanfoug, L. M. Augustin, Y. Barbarin, J. J. G. M. van der Tol, E. A. J. M. Bente, F. Karouta, D. Rogers, S. Cole, Y. S. Oei, X. J. M. Leijtens, and M. K. Smit, "Reduced reflections from multimode interference couplers," *Electron. Lett.*, vol. 42, no. 8, pp. 465–466, Apr. 2006.
[17] A. Poustie, "Hybrid integration for advanced photonic devices," in *Proc. SPIE*, 2008, vol. 7135, pp. 713502-1–713502-10.
[18] M. J. R. Heck, A. la Porta, X. J. M. Leijtens, L. M. Augustin, T. de Vries, E. Smalbrugge, Y. S. Oei, R. Nötzel, R. Gaudino, D. J. Robbins, and M. K. Smit, "Monolithic AWG-based discretely tunable laser diode with nanosecond switching speed," *IEEE Photon. Technol. Lett.*, vol. 21, no. 13, pp. 905–907, Jul. 2009.
[19] Y. Barbarin, E. A. J. M. Bente, M. J. R. Heck, J. H. den Besten, G. Guidi, Y. S. Oei, J. J. M. Binsma, and M. K. Smit, "Realization and modeling of a 27-GHz integrated passively mo de-locked ring laser," *IEEE Photon. Technol. Lett.*, vol. 17, no. 11, pp. 2277–2279, Nov. 2005.
[20] Y. Barbarin, E. A. J. M. Bente, C. Marquet, E. J. S. Leclère, J. J. M. Binsma, and M. K. Smit, "Measurement of reflectivity of butt-joint active-passive interfaces in integrated extended cavity lasers," *IEEE Photon. Technol. Lett.*, vol. 17, no. 11, pp. 2265–2267, Nov. 2005.
[21] F. Morichetti, A. Canciamilla, C. Ferrari, M. Torregiani, A. Melloni, and M. Martinelli, "Roughness induced back-scattering in optical silicon waveguides," *Phys. Rev. Lett.*, vol. 104, no. 3, pp. 033902-1–033902-4, Jan. 2010.